Correlating Electronic Transport and 1/*f* Noise in $MoSe_2$ Field-Effect Transistors

Jiseok Kwon,[1,2] Abhijith Prakash,[1,2] Suprem R. Das,[3,4,*] and David B. Janes[1,2,†]

[1] *School of Electrical and Computer Engineering, Purdue University, West Lafayette, Indiana 47907*
[2] *Birck Nanotechnology Center, Purdue University, West Lafayette, Indiana 47907*
[3] *Department of Industrial and Manufacturing Systems Engineering, Kansas State University, Manhattan, Kansas 66506*
[4] *Department of Electrical and Computer Engineering, Kansas State University, Manhattan, Kansas 66506*

(Received 4 February 2018; revised manuscript received 19 June 2018; published 12 December 2018)

Two-Dimensional Transition Metal Dichalcogenides (2D TMDCs) such as MoS_2, $MoSe_2$, WS_2, and WSe_2 with van der Waal's type interlayer coupling are being widely explored as channel materials in a Schottky Barrier Field Effect Transistor (SB FET) configuration. While their excellent electrostatic control and high *on*/*off* ratios have been identified, a clear correlation between electronic transport and the low-frequency noise with different atomic-layer thickness is missing. For multilayer channels in MoS_2 FETs, the effects of interlayer-coupling resistance on device conductance and mobility have been studied, but no systematic study has included interlayer effects in consideration of the intrinsic (channel) and extrinsic (total device) noise behavior. Here, we report the 1/*f* noise properties in $MoSe_2$ FETs with varying channel thicknesses (3–40 atomic layers). Contributions of channel vs access/contact regions are extracted from current-voltage (transport) and 1/*f* noise measurements. The measured noise amplitude shows a direct crossover from channel- to contact-dominated noise as the gate voltage is increased. The results can be interpreted in terms of a Hooge relationship associated with the channel noise, a transition region, and a saturated high-gate-voltage regime whose characteristics are determined by a voltage-independent conductance and noise source associated with the metallurgical contact and the interlayer resistance. Both the channel Hooge coefficient and the channel/access noise amplitude decrease with increasing channel thickness over the range of 3–15 atomic layers, with the former remaining approximately constant and the latter increasing over a range of 20–40 atomic layers. The analysis can be extended to devices based on other TMDCs.

DOI: 10.1103/PhysRevApplied.10.064029

I. INTRODUCTION

Two-dimensional (2D) atomic crystals, especially transition metal dichalcogenides (TMDCs) such as MX_2 ($M \equiv$ Mo, W and $X \equiv$ S, Se) have shown fascinating electronic and optical properties and are of interest for future nanoelectronic, optoelectronic, and nanophotonic devices [1–4]. Multilayer TMDC materials show layer stacking via van der Waal interaction between layers. Characteristics such as an indirect-to-direct band-gap crossover [5,6], formation of strongly correlated many-body bound states in monolayers [7–9], and tunability in band gaps between 1.0 and 2.0 eV make 2D TMDCs attractive for fundamental as well as applied research [10–14]. A number of TMDCs have been used as channel materials in field effect transistors (FETs), yielding devices with low off current, an *on*/*off* ratio above 10^6, high-field-effect mobility, and near 60 mV/decade subthreshold swings [15–19]. There are also recent demonstrations of fully integrated circuits and logic-building blocks (such as an inverter, NAND gate, static RAM, and five-stage ring oscillator) from 2D FET devices [20–25].

Contacts play a very important role in the charge injection process into the channel of a back-gated SB FET, particularly for the metal source/drain contacts typically employed with TMDCs [10,26]. In a study on MoS_2 FETs comparing contact metals with various work functions, Das et al. [17] showed a significant change in extrinsic mobility over the range of work functions, with the highest performance observed for the lowest work function material (scandium). There have been detailed transport measurements focused on microscopic analysis of channel materials as well as channel-metal contact effects (both room and low temperature) [27,28]. Low-frequency (1/*f*) noise, a ubiquitous phenomenon in every electronic device, has not been well understood and correlated to transport features in these 2D FET devices.

*srdas@ksu.edu
†janes@purdue.edu

 © 2018 American Physical Society

Low-frequency ($1/f$) noise, a fundamental technique in characterizing semiconducting materials and devices [29–31], has also become valuable in characterizing nanoscale materials and devices, shedding light on the microscopic origin of transport fluctuations, and providing a means to evaluate electronic states at the channel/dielectric interface. Low-frequency device noise can also have significant implications on circuits and systems (such as circuits for rf communications). The noise properties are dependent on the interaction of carriers with the channel/dielectric interface states as well as the contact and access-region properties. Therefore, it is essential to characterize the $1/f$ noise of devices consisting of low-dimensional materials such as nanowires, carbon nanotubes, graphene, and TMDCs [32–38]. Furthermore, 2D van der Waal channel materials (graphene, TMDCs) are expected to show unique noise characteristics due to the existence of interlayer resistances between the individual ultrathin channel layers and the presence of grain boundaries as transport barriers in the case of large-scale 2D channels (typically grown using CVD techniques). Indeed, in recent studies, some of these features have been demonstrated in noise characteristics: for example, the contrasting nature of $1/f$ noise in single-layer graphene (SLG) and bilayer graphene (BLG) has been studied by Min et al. and interpreted in terms of their unique band structure [39]. There are several reports of noise in transistors with TMDC channels. The impact of strong localization with a five-order of magnitude higher $1/f$ noise along the grain boundaries of CVD MoS_2 compared to the intergrain noise has been shown recently by Hsieh et al. [40]. In prior studies on noise in various TMDC transistors, the gate-voltage and/or current dependences have been interpreted in terms of various noise mechanisms, including McWhorter (number fluctuation) model, Hooge (mobility fluctuation) model, or a transition from Hooge to McWhorter models [37,41–43]. Some prior studies in TMDC FETs with relatively thin channel layers have shown behavior consistent with a McWhorter model, either within a channel-dominated regime above threshold [44] or over a bias-range-spanning subthreshold and above threshold (e.g., weak vs strong "inversion"), but without explicitly considering contact effects [43]. However, other studies have observed behavior that is consistent with a Hooge mechanism over a significant gate voltage range (above threshold voltage) [37,45]. A combined number of fluctuation/correlated mobility fluctuation models have also been discussed [41,42]. Na et al. [41] studied unpassivated and passivated MoS_2 devices (approximately 18 layers) and analyzed the results with a mixture of Hooge and McWhorter models, but observed Hooge behavior in "bulk" (approximately 62 layers) devices. Other studies also showed the interpretation with the unified model of carrier-number fluctuation and correlated mobility fluctuations in single-layer CVD [46] and thick-layer (75 layers) TMDC FETs [47]. A transition from Hooge regime to McWhorter regime with increasing I_d in these studies generally ignores the contact effects, which could be responsible for the observed transition in noise behavior. In general, these studies indicate that noise behavior is different in strong vs weak "inversion" regimes and that increased layer thicknesses yield lower noise than single-/few-layer devices. However, it is difficult to draw specific conclusions regarding what device parameter or material choice yields a specific dominant noise mechanism. For example, Hooge behavior is observed for thin layers (monolayer and bilayer) in some cases, but for bulk layers in other studies [48]. Some studies have considered contact and channel effects [44,49], but consideration of noise properties vs layer thickness has been limited and a comprehensive model for layer-thickness dependence is not available. A more thorough understanding of $1/f$ noise behavior, including consideration of channel thickness and contributions of contacts, should enable better device structures, which will be important for sensors [50] and digital and analog electronics [51], as well as linear circuits for rf communications [52].

The current study focuses on multilayer $MoSe_2$ FET devices with channels of various atomically controlled thicknesses. Analogous to MoS_2, $MoSe_2$ shows a tunable energy gap and crossover from indirect to direct band gap in the monolayer limit [53–55], However, in our observation, $MoSe_2$ FETs show higher ambient stability for prolonged duration with minimal hysteresis during forward- and reverse-bias conditions. Several other unique characteristics of $MoSe_2$ over MoS_2 are (1) degenerate indirect and direct band gap with decoupling of bulk and 2D limit [55]. (2) Angle-resolved photoemission spectroscopy (ARPES) shows that the dispersion of the valence bands decreases along the $k_{\parallel}$ and $k_{\perp}$ directions, indicating an increased 2D character (or increased interlayer distance) [56]. (3) $MoSe_2$ shows a much weaker bound exciton peak compared to MoS_2, therefore, having a faster photoresponse time (approximately three-orders of magnitude faster; 25 ms compared to <30 s for MoS_2) than MoS_2, indicating potential applications in efficient phototransistors [57]. (4) The atomic defects (Mo-Se defects) in $MoSe_2$ are reported to be less significant than the Mo-S defects in MoS_2 [58]. These properties, along with the observed transistor characteristics, make $MoSe_2$ a promising material for nanoelectronic and optoelectronic device applications. While the transport properties of $MoSe_2$ FETs have been reported, $1/f$ noise characterization has not been considered in detail, e.g., to include consideration of the channel and contact noise in terms of the channel thickness [49,59].

Herein, we present an experimental study of the current-voltage relationships and gate-bias-dependent $1/f$ noise in $MoSe_2$ transistors with channel thicknesses varying from 3 to 40 atomic layers. For a given layer thickness, the

gate-bias dependences of both the conductance and noise at low-drain fields (linear regime) can be understood in terms of noise contributions and conductance from the channel and contact/access regions. The model developed in the current work can fit voltage dependence without the need to assume a voltage-variable noise mechanism within the channel. Our study shows that the voltage dependence can be fit by a model considering a transition from channel-dominated noise to contact-dominated noise, and that a single noise mechanism is satisfactory to explain the channel contribution to noise. Comparison of the properties of devices with varying layer thicknesses allows both qualitative and quantitative comparison of the intrinsic channel properties (mobility and Hooge parameter) and the contributions from the contact- and interlayer-coupling resistances. As the layer thickness increases over the range of 3–15 monolayers, the mobility increases and noise amplitude decreases, consistent with decreasing interactions between carriers and interface states. For thicknesses of 20 layers and beyond, increasing layer thickness leads to decreased extrinsic mobility and increased noise amplitude, associated with increased series resistance involved with interlayer-coupling resistance.

II. EXPERIMENTAL DETAILS

$MoSe_2$ layers of various atomic thicknesses are exfoliated on Si/SiO_2 (90 nm) substrates using a mechanical exfoliation method and their locations are identified using predefined alignment markers on the Si/SiO_2 substrates. Precisely, $MoSe_2$ layers with 3L, 5L, 8L, 10L, 15L, 20L, and 40L are selected for FET-device fabrication. L stands for a single molecular layer of $MoSe_2$ solid. High-quality bulk $MoSe_2$ crystals (from 2D Semiconductor, Inc.) are used to obtain the above flakes with mechanical exfoliation. The thicknesses of the flakes are determined by AFM and the quality of the flakes is evaluated using Raman spectroscopy (with a laser-excitation wavelength of 532 nm). Source and drain (*SD*) contact electrodes of 50-nm-thick nickel are used in the transistor structure. The channel length of each of the devices is kept at 2 μm and the channel widths, determined by the flake dimension, are kept at approximately between 2 and 4 μm. A semiconductor parameter analyzer, electrical probe station, and arrangements for 1/*f* noise measurements are used for the transport- and noise-characteristics study of all of the above FETs. More details of the device fabrication and measurement set up are provided in Appendix A.

III. RESULTS AND DISCUSSION

Figure 1(a) shows the schematic view of the nickel *SD* and back-gated $MoSe_2$ FET structure studied in this study. Figure 1(b) shows the AFM image and step profile of a representative $MoSe_2$ flake that forms the channel of a FET with a thickness of around 9.7 nm, corresponding to approximately 15 molecular layers (single-layer thickness of $MoSe_2 \sim 0.65$ nm) [60]. Figure 1(c) shows the Raman spectrum of a representative flake (15 layers) acquired near its center (the laser spot size is approximately 1 μm in diameter and hence could be well focused at the center of the flake whose area is a few square micrometers). The two primary Raman peaks, measured at positions of 243.42 and 286.32 cm^{-1}, are assigned to the A_{1g} and E^1_{2g} vibrational modes, corresponding to the out-of-plane and in-plane lattice vibrations, respectively.

The electrical characteristics are measured in ambient conditions with electromagnetic and light shielding (see Appendix A for more details). Note that the devices studied in the present work are back-gated SB FETs having a fraction of the channel itself buried underneath the *SD* contacts, consequently the contribution of these portions in

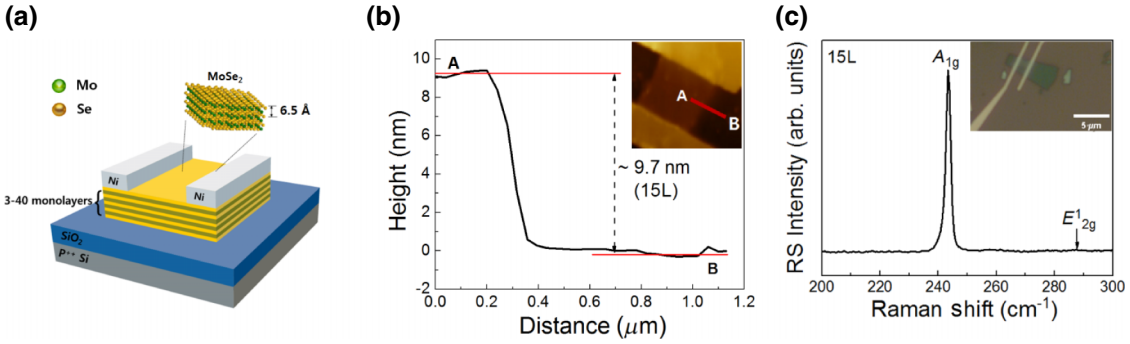

FIG. 1. (a) A schematic view of $MoSe_2$ field-effect transistor employed in the present work. $MoSe_2$ flakes with various numbers of atomic layers are used as transistor channels. The nickel-*SD*-contact electrodes are fabricated on top of the back-gated channel. (b) AFM image and geometrical step profile of a $MoSe_2$ flake within a representative field-effect-transistor channel. The thickness of the $MoSe_2$ layer is approximately 9.7 nm, corresponding to approximately 15 layers. (c) The corresponding Raman spectrum of a $MoSe_2$ flake is shown collected using a 532-nm excitation source. The presence of two principal peaks, A_{1g} and E^1_{2g}, confirms a bonding environment corresponding to $MoSe_2$. The inset shows the optical microscope image of the device used in this study.

the carrier transport is critical for the device analysis [10]. Models which include the impact of these channel segments on carrier transport in both the *off* state [10] and the *on* state [26] have been reported previously for WSe_2 FETs and MoS_2 FETs, respectively. In the present work on $MoSe_2$ FETs, we follow the *on*-state model for the transport data analysis and discussion [26].

Figure 2(a) shows the measured low-field (drain-source voltage (V_{DS}) of 0.2 V) transfer characteristics of FETs with the indicated layer thicknesses. At a given gate-source voltage (V_{GS}), the drain current (I_d) increases with increasing layer thickness over the range of 3L–15L. The 20L and 40L devices show a saturation with increasing V_{GS}, consistent with the series-resistance effects. A similar trend in drain current maxima has been reported in MoS_2 FETs with low Schottky barrier height electrodes, with an approximately 9L-thick channel producing the optimum current [27]. The threshold voltage (V_{th}) of each of the devices is obtained by extrapolating the low-field I_d-V_{GS} relationship to $I_d = 0$.

The transconductance ($g_m = dI_{DS}/dV_{GS}$) is dependent on V_{GS}; the maximum value is used to calculate the extrinsic mobility ($\mu_{ext.}$) at the low-drain field ($V_{DS} = 0.2$ V), using

$$\mu_{ext} = \frac{dI_{DS}}{dV_{GS}} \times \frac{L}{W} \times \frac{1}{C_{ox}} \times \frac{1}{V_{DS}} \tag{1}$$

where L and W are the channel length and width, respectively, and C_{ox} is the gate oxide capacitance per unit area (3.84×10^{-4} F/m^2 for 90-nm SiO_2). (The extraction of $\mu_{ext.}$ is described in Appendix C) Figure 2(b) shows the measured $\mu_{ext.}$ and the intrinsic mobility (μ_{int}, discussed later) as functions of $MoSe_2$ layer thickness. The rise of extrinsic-field-effect mobility with channel thickness (number of layers), observation of a maximum value (between 8L and 15L), and decrease beyond 15L indicates the dominant role of the access resistances arising from *SD* contacts and the interlayer coupling beyond 15L. Comparable behavior has been observed by Das et al. in MoS_2 transistors and analytically modelled using a resistance network model [26].

The measured *I-V* relationships and $\mu_{ext.}$ reflect extrinsic values, i.e., they contain contributions from series resistance (R_1) as well as from the channel. The total extrinsic resistance, R_{total}, is the sum of R_1, which is expected to be independent of V_{GS} in the *on* state, and the channel resistance (R_{ch}), i.e.,

$$R_{total} = R_1 + R_{ch}. \tag{2}$$

R_1 is calculated from the intercept of the relationship between R_{total} and the inverse of V_{GS}-V_{th} (shown in Appendix B) [61]. The extracted values of R_1 and R_1 normalized by W are shown for devices with various thicknesses in Table I. Given the nature of the 2D van der Waal's solids, in general, R_1 will contain contributions from the metal-semiconductor contact resistance (R_S) as well as the interlayer-coupling resistance (R_{int}) between n number of layers. In a limit in which n is significantly larger than the number of layers contributing to channel conductance, one would expect a relationship comparable to

$$R_1 = R_S + nR_{int} \tag{3}$$

In order to quantify the channel behavior, one needs to obtain intrinsic values, i.e., without the effects of contacts/access resistances. To calculate μ_{int}, the actual drain voltage across the channel (V'_{DS}) is calculated using

$$V'_{DS} = \frac{V_{DS}(R_{total} - R_1)}{R_{total}} \tag{4}$$

and

$$\mu_{int} = \frac{dI_{DS}}{dV_{GS}} \times \frac{L}{W} \times \frac{1}{C_{ox}} \times \frac{1}{V'_{DS}} \tag{5}$$

where n is the number of $MoSe_2$ layers and R_{int} is the interlayer resistance. As shown in Fig. 2(b), following this correction, $\mu_{int.}$ remains relatively constant for layer thicknesses above 15L (approximately 55 cm^2/V·s). For layer thicknesses below 15L, μ_{int} increases with increasing layer thickness. As discussed in prior studies, in few-layer devices, carrier scattering in the channel impacts the

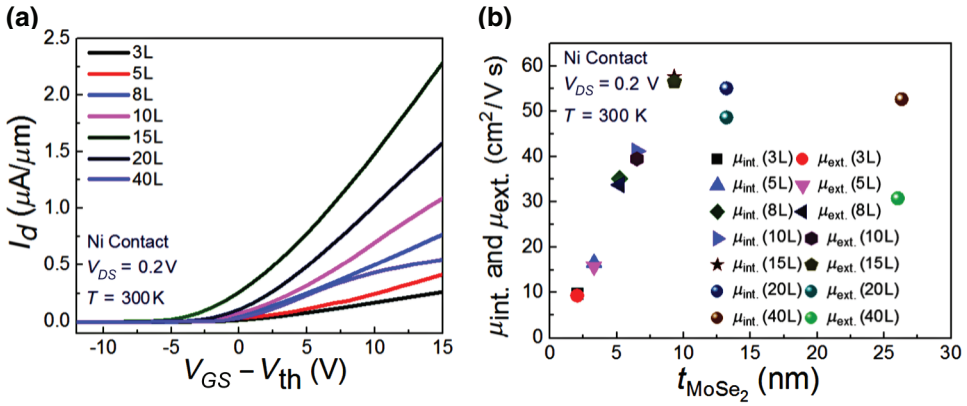

FIG. 2. Characteristics of $MoSe_2$ FETs with different layer thicknesses ($N = 3$, 5, 8, 10, 15, 20, and 40L), including, (a) transfer characteristics measured at $V_{DS} = 0.2$ V. (b) Intrinsic and extrinsic field-effect mobilities extracted at $V_{DS} = 0.2$ V as a function of the $MoSe_2$ layer thickness. For the 8L device, parameters are presented for the 2-μm-channel length.

TABLE I. The electrical transport parameters and noise parameters of $MoSe_2$ field-effect transistors with various channel thicknesses studied in this work.

No. of layers	V_{th}	$L_{ch}(\mu m) \times W_{ch}(\mu m)$	R_1 (kΩ)	$R_1 \times W_{ch}$ (Ω mm)	S_{R1} (Ω^2/Hz)	α_H	Voltage of Cross Point (1st and 2nd terms)
3L	9 V	1.9×3	141	423	1014	7.08×10^{-1}	20 V
5L	17 V	2×1.8	210	378	925.5	2.61×10^{-1}	17 V
8L	10 V	0.5×3	12	36	0.33	9.83×10^{-3}	22 V
8L	12 V	1×3	20	60	0.82	9.24×10^{-3}	20 V
8L	13 V	2×4	32	128	2.09	9.47×10^{-3}	19 V
10L	18 V	1.9×2.1	54.2	113.8	5	5.25×10^{-3}	16 V
15L	13 V	2×1.8	21	37.8	0.275	2.64×10^{-3}	19 V
20L	10 V	2×1.9	30	57	0.77	4.58×10^{-3}	20 V
40L	11 V	1.8×2.2	187	411	137	1.54×10^{-2}	9 V

current injection as well as the mobility [26]. A number of atomic layers are required to screen such scattering effects and achieve the optimal mobility. Beyond this thickness, $\mu_{int.}$ should remain relatively constant, as is observed. However, R_1 increases with increasing layer thickness due to the effects of interlayer coupling, which leads to a decreasing μ_{ext}.

The 1/f noise characteristics, a ubiquitous yet a key limiting factor that needs to be addressed in low-dimensional electronic devices, are of interest in terms of both the properties of the channel, e.g., channel-oxide interface, and the contributions from series resistance. Absence of such a study systematically in 2D TMDC devices, particularly the one relating to the transport and noise in the same devices and with number of atomic layer channel thicknesses, would provide a direct correlation among these parameters insisting better and accurate design considerations of such devices for optimal performance.

Figure 3(a) shows the normalized noise-current spectral density (S_I/I_d^2) vs frequency (f) between 1 Hz and 1 kHz for $MoSe_2$ FETs with various channel thicknesses. The measurements are performed at $V_{DS} = 50$ mV (to maintain operation in the linear regime) and an overdrive voltage ($V_{GS} - V_{th}$) of 7 V for all the devices. All the FETs follow a nominal 1/f relationship (dotted line). Figure 3(b) shows the total noise amplitude ($f \times S_I/I_d^2$), along with the channel and contact/access contributions (discussed later), at $f = 100$ Hz vs the number of layers. The total noise clearly demonstrates a significant decrease of 1/f noise with increasing channel thickness up to 15L. Beyond 15L, the total device noise increases gradually. The behavior for a small number of layers is consistent with significant scattering from impurities and/or interface states (localized electronic states and Coulomb potentials from the substrate have been proposed earlier [62]). As the layer number increases to 15, the channel screens such effects (observation of a charge-transport localization within several layers in TMDC channels has been previously shown [63]). Moreover, the increase in the total device noise beyond 15 layers most likely is associated with access resistances involving the contact resistances, excess channel resistances, and interlayer coupling.

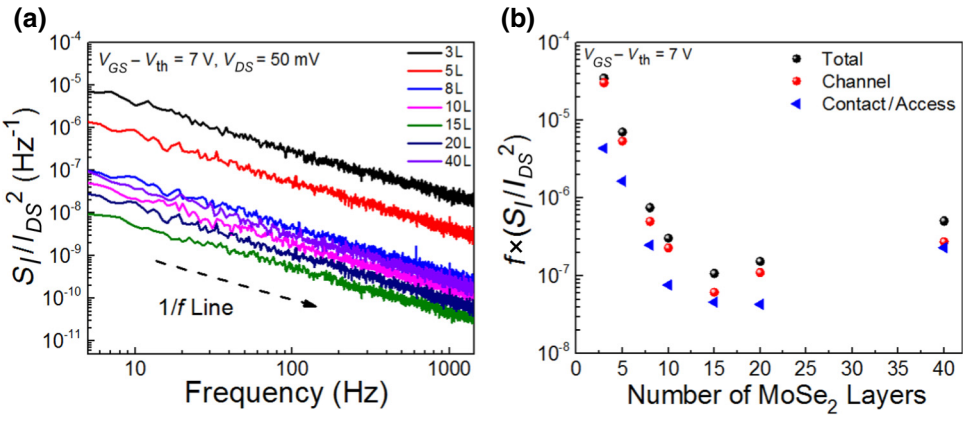

FIG. 3. (a) 1/f noise-current-power-spectral density for FETs with different numbers of $MoSe_2$ layers as a function of frequency for various numbers of layers and (b) comparison of normalized noise amplitudes (total noise, channel noise, contact/access noise) for FETs with different numbers of $MoSe_2$ layers. Noise measurements are performed at $V_{GS} - V_{th} = 7$ V, frequency of 100 Hz, and at low-drain bias ($V_{DS} = 50$ mV) and channel vs contact/access contributions are extracted as described in the text.

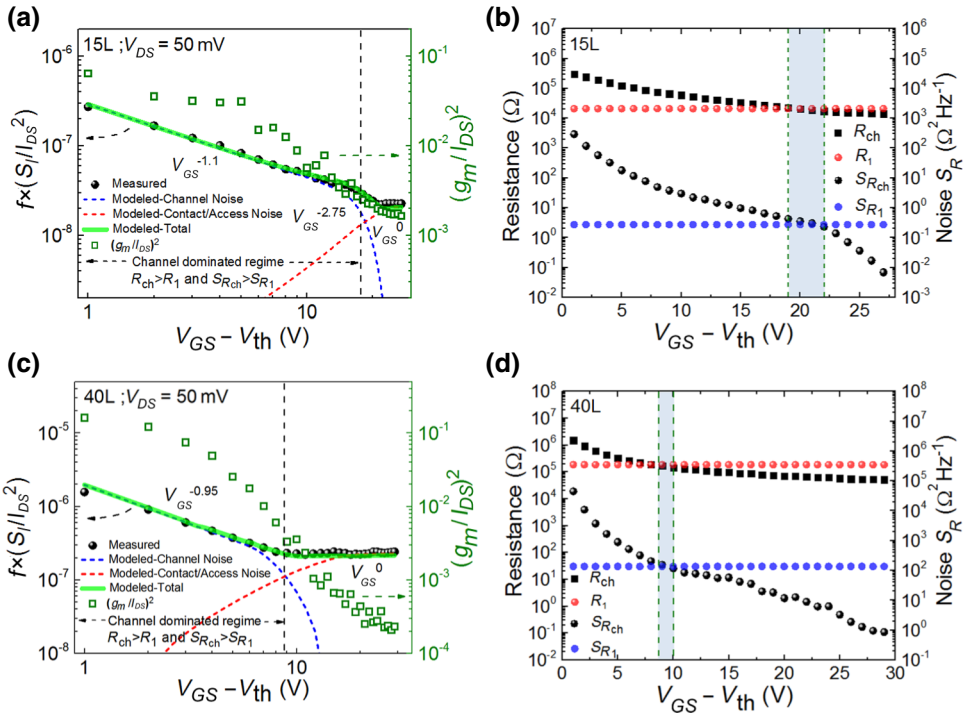

FIG. 4. (a) Measured and modeled $1/f$ noise response of 15L $MoSe_2$ FET. The round symbols represent the measured data points for the normalized noise-current-power-spectral density, $f \times S_I/I_{DS}^2$, as a function of the gate bias. The dashed lines represent the model fitting for the noise dominated by the channel contribution and the contact contribution, respectively. The green line shows the sum of both contributions. Green opened square corresponds to $(g_m/I_{DS})^2$ in the right-sided y axis. The agreement between the modeled fitting and measured data indicates that the measured voltage dependence can be explained by a channel following Hooge's mobility-fluctuation model, with a transition to a contact/access-dominated regime. (b) Contact and channel components of the noise and resistance for 15L $MoSe_2$ FET, obtained from measurements using procedure described in the text. Blue area represents "transition regime" in which channel dominates noise, but contact/access regions dominate resistance. (c) Measured, modeled $1/f$ noise response and $(g_m/I_{DS})^2$ of 40L $MoSe_2$ FET, using same symbols as (a). (d) Contact and channel components of the noise and resistance for 40L $MoSe_2$ FET, using same symbols as (b). In comparison to 15L FET, the transition voltages are lower, and the width of the transition region is smaller. The noise amplitudes of the channel-dominated regime (at the same bias point) and the contact/channel-dominated regime are also larger, corresponding to a larger Hooge parameter and an increased noise contribution from interlayer resistances, respectively.

Figures 4(a) and 4(c) show the measured noise amplitude vs $(V_{GS} - V_{th})$ for representative $MoSe_2$ FETs (15L and 40L, respectively, black solid circles). In order to allow comparison to the experimental data, the corresponding model (discussed later) is also shown, with blue and red dotted lines representing the terms associated with the channel and contact noise sources, respectively, and the green line representing the overall model. In order to compare our experimental data and model to that expected from a McWhorter model, we include $(g_m/I_d)^2$ vs $V_{GS} - V_{th}$ curves in the same plots for 15L and 40L FETs. Corresponding figures for devices with all other channel thicknesses discussed in this work are shown in the appendix Fig. 9. Over the voltage range considered, the $(g_m/I_d)^2$ relationship exhibits a different gate-voltage dependence than the experimental noise amplitude. For layer thicknesses above 8L, this effect is prominent even if one restricts the voltage range to the channel-dominated regime. Similar conclusions can be reached if one considers the $(V_{GS} - V_{th})^{-2}$ dependence associated with a McWhorter mechanism [43,44]; such behavior is not observed in the experimental data. The model considered in this study, which utilizes a Hooge noise model plus contact effects, fits the data much better than a McWhorter model.

For overdrive voltages below approximately 10 V (approximately 9 V) for 15L (40L), the data approximately follows an inverse relation with overdrive voltage, as expected for noise dominated by mobility fluctuation (Hooge model) [32,64]. At large overdrive voltages, the noise amplitude saturates as expected in regimes in which the series resistance dominates both noise and resistance [32,44,64]. Qualitatively similar behavior is observed for the FETs with other thicknesses in this study (see appendix FIG. 9 showing results for 3L, 5L, 8L, 10L, and 20L). The dependencies on both voltage and layer thickness can be explained using a model that considers

the effects of both the channel and the series resistance, as shown by the green curve in Figs. 4(a) and 4(c) and explained in the following section.

As with the conductance/mobility behavior, the noise behavior can be separated into contributions from the channel and from the series resistance. Following previous approaches for separating channel and contact-noise contributions in transistors [32,44,65], it is convenient to transform them into resistance-spectral-power density for the overall device ($S_{R\text{total}}$) and to consider contributions of noise sources and resistances associated with the channel and series resistance:

$$\frac{S_I}{I_d^2} = \frac{S_{R\text{total}}}{R_{\text{total}}^2} = \frac{S_{R1} + S_{R\text{ch}}}{(R_1 + R_{\text{ch}})^2}, \tag{6a}$$

which can be rearranged to

$$\frac{S_I}{I_d^2} = \frac{S_{R1}}{R_1^2}\frac{R_1^2}{(R_1 + R_{\text{ch}})^2} + \frac{S_{R\text{ch}}}{R_{\text{ch}}^2}\frac{R_{\text{ch}}^2}{(R_1 + R_{\text{ch}})^2}, \tag{6b}$$

Here, $S_{R\text{ch}}/R_{\text{ch}}^2$ and S_{R1}/R_1^2 are the normalized noise-resistance power-spectral densities for the channel and series (contact and interlayer) resistances, respectively. For each device, the parameters on the right side of Eq. (6b) are extracted at a common V_{DS} (0.2 V) as follows. For resistances, R_{total} is determined at each V_{GS} (above threshold) from the corresponding measured I_{DS}. R_1 is determined as stated earlier and assumed to be independent of V_{GS}. At each V_{GS}, $R_{\text{ch}}(V_{GS})$ is determined from $R_{\text{total}}(V_{GS})$ and R_1, using Eq. (2). Figure 4(b) shows the extracted $R_{\text{ch}}(V_{GS})$ and R_1 for the representative 15L device, along with the corresponding noise power densities (discussed layer). A crossover from channel-dominated ($R_{\text{ch}} > R_1$) to series-resistance dominated ($R_{\text{ch}} < R_1$) behavior is observed at approximately V_{GS}-$V_{\text{th}} = 19$ V (additional devices shown in Appendix D). Such a transition for a 40L $MoSe_2$ FET is shown in Fig. 4(d) with the resistance crossover point at a much lower voltage (approximately 9 V).

The total noise amplitude, e.g., the data in Figs. 4(a) and 4(c) for 15L and 40L, respectively, is used along with the resistances R_{total}, R_1, and R_{ch} to calculate the noise sources S_{R1} and $S_{R\text{ch}}$. First, the Hooge parameter is extracted using the small overdrive voltage regime, in which the measured S_I/I_d^2 exhibits a voltage dependence of approximately $(V_{GS} - V_{\text{th}})^{-1}$, and therefore, $S_{R\text{ch}} >> S_{R1}$ is a reasonable assumption. Next, the value of $S_{R\text{ch}}$ at the maximum measured overdrive voltage is calculated using the Hooge relationship. The value of S_{R1} is obtained by evaluating Eq. (6b) at this voltage, i.e., using the bias-independent R_1 and the R_{ch}, $S_{R\text{ch}}$, and measured S_I/I_d^2 values corresponding to this voltage. Finally, $S_{R\text{ch}}$ is determined at other gate voltages using Eq. (6b), with the corresponding R_{ch} and measured S_I/I_d^2 values. The extracted S_{R1} and $S_{R\text{ch}}$ values for the representative 15L device and 40L device are shown in Figs. 4(b) and 4(d), respectively, and for devices with other thicknesses in Appendix D. Several regimes are observed. For modest $(V_{GS} - V_{\text{th}})$ values, the total noise is dominated by the $S_{R\text{ch}}$ term and follows a Hooge relationship, as evidenced by a gate-voltage dependence close to $(V_{GS} - V_{\text{th}})^{-1}$. A noise crossover point ($S_{R\text{ch}} = S_{R1}$) is observed, occurring at approximately $V_{GS} - V_{\text{th}} = 21.5$ V for the 15L device. The region between the resistance crossover point and the noise crossover point, as indicated by the shaded region in Fig. 4(b), represents a transition region in which ($R_{\text{ch}} < R_1$), but ($S_{R\text{ch}} > S_{R1}$). Within this region, the noise amplitude is expected to follow a voltage relationship different from either the low V_{GS} (channel-dominated) regime or the high V_{GS} (series-resistance-dominated) limit [31,64]. For the 40L device, a qualitatively similar behavior is observed [Fig. 4(d)], but with a noise crossover voltage at approximately $V_{GS} - V_{\text{th}} = 10$ V and a much narrower transition region. The effect of the narrower transition region is evident in Fig. 4(c) where there is distinct variation from channel-dominated to contact-dominated noise regimes without a clear intermediate V_{GS} dependence. The availability of noise and resistance parameters allows calculation of the overall voltage dependence of the noise amplitude using Eq. (6b). Figures 4(b) and 4(d) show the contact/access [first term in Eq. (6b)] and channel (second term) contributions to the noise amplitude, along with the overall amplitude (sum of the two terms) for 15L and 40L devices, respectively. Comparable plots for devices with other layer thicknesses are shown in the appendix. The overall amplitude, i.e., full right side of Eq. (6b) (green line), matches well with the measured value over the entire voltage range. For overdrive voltages below approximately 15V, the behavior is dominated by the channel contribution and follows a $V_{GS}^{-1.1}$, consistent with a mobility-fluctuation (Hooge) noise model. The channel contribution rolls off for V_{GS} values above approximately 15 V due to the resistance factor in the second term of Eq. (6b); R_{ch} is monotonically decreasing while R_1 remains constant. The collective effect of the resistance and S_R transitions is a transition region in the noise amplitude, with approximately $V_{GS}^{-2.75}$ dependence for this representative device. For voltages beyond this transition region, V_{GS}^0 behavior is observed, as expected for a regime in which the series resistance dominates both noise and resistance. Similar channel and noise data extraction analyses are performed for all the devices, and the corresponding values are listed in Table I.

The extracted channel, series resistance, and total noise amplitudes are plotted along with the corresponding measured data in Fig. 5(a). All the devices show a clear transition from a region following the Hooge relationship to a V_{gs}^0 regime. However, the relationships are quantitatively different with respect to changes in transition

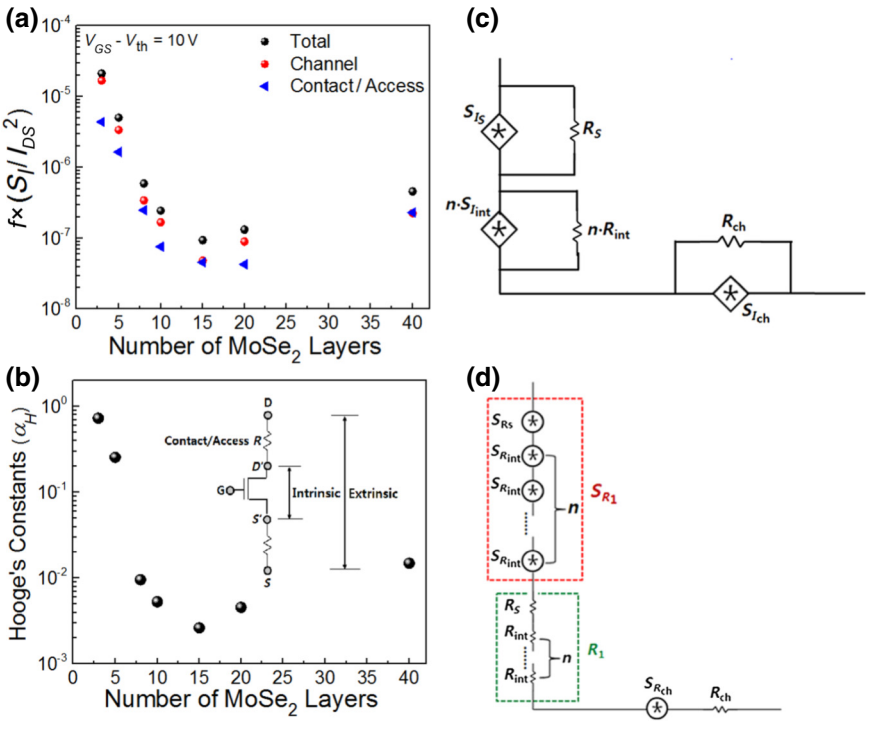

FIG. 5. Comparison of noise parameters at 10-V-overdrive voltage (a) The comparison of normalized noise amplitudes (total, channel, contact/access) for FETs with different numbers of $MoSe_2$ layers. All the noise measurements are performed at $V_{GS} - V_{th} = 10$ V, frequency of 100 Hz, and low-drain bias ($V_{DS} = 50$ mV). (b) Hooge's constants (α_H) as a function of number of layers in $MoSe_2$ FETs. The inset shows schematic representation of the intrinsic and extrinsic FETs. (c) Representation of total noise originating from three independent current-noise sources, namely, contact resistance, interlayer-coupling resistance, and the channel resistance. (d) Thevenin equivalent-resistance-noise sources are shown.

voltages, voltage range, and limiting values. In order to allow comparison of the channel and contact/access contributions to noise at a common bias point, the normalized noise amplitudes, transformed back to S_I/I_d^2 using Eq. (6b), are plotted for an overdrive voltage of 7 V in Fig. 3(b). This overdrive voltage allows comparisons of all devices in the regime in which the channel-noise term dominates, although the 40L device is at a bias point at which the R_1 term starts to contribute. As observed in Fig. 3(b), the contact/access contribution is smaller than the channel term for all devices, as expected based on the choice of overdrive voltage. Qualitatively similar behavior is expected at other bias points within the channel-dominated regime. The observation of a contact/access contribution that decreases significantly with layer thickness (3L–15L) is consistent with an overall decrease in series resistance over that regime. The increase in this noise contribution at larger layer thicknesses is qualitatively consistent with the expected dependence of adding noise sources corresponding to interlayer coupling resistances, both in terms of the observed increase in R_1 and the additional noise-power-spectral density (S_{R1}). However, as evidenced by the dependence of R_1 values vs layer thickness, which does not follow the simple model described in Eq. (3), attributing specific contributions to metallurgical contact vs interlayer resistance effects is somewhat difficult.

The observation of a clear channel-dominated regime, which follows the Hooge relationship [29,49],

$$\frac{S_I}{I_d^2} = \frac{\alpha_H}{f \times N}, \tag{7}$$

where S_I is the current-noise-power-spectral density, I_d is the drain current in the channel, f is the frequency, and $N = (C_{ox}/q) \times (V_{gs} - V_{th}) \times LW$ is the total number of charge carriers in the channel, allows quantitative comparison of channel-noise properties through the α_H values. In this regard, a rearrangement of Eq. (7) in the channel-dominated regime gives

$$f \times \frac{S_I}{I_d^2} = f \times \frac{S_{Rch}}{R_{ch}^2} = \frac{q \times \alpha_H}{C_{ox} \times LW} \times \frac{1}{(V_{GS} - V_{th})}. \tag{8}$$

Using Eq. (8), the Hooge parameter, α_H, (quantifying channel-noise property and excluding effects of R_1 and S_{R1}) can be extracted from linear fitting within the channel-dominated regime, i.e., the region of Figs. 4(a) and 4(c) showing a slope of approximately V_{gs}^{-1}. This analysis yields an α_H value for each layer thickness. The corresponding values are tabulated in Table I, along with values of R_1 and S_{R1}, which describe the contact/access resistance parameters. The Hooge's parameter vs atomic layer number is shown in Fig. 5(b). Hooge's constants are extracted in the voltage region in which the channel is dominating both noise and resistance, i.e., in which the term containing S_{Rch} and R_{ch} dominates. The Hooge parameter is considered to be a figure of merit for the channel region and should be independent of contact/access resistances. Broadly, the decrease in Hooge parameter with increasing layer thickness (3L–15L) can be attributed to decreasing interactions of the channel charge with oxide/interface trap states. Beyond 15L, the centroid of the channel distribution is not expected to change significantly, as evidenced

by a relatively constant intrinsic mobility, so the Hooge parameter and the channel/interface trap interaction are expected to remain relatively constant. Figure 5(c) illustrates the equivalent-circuit model involving the case of a channel-noise-current source ($S_{I\mathrm{ch}}$) in series with noise-current sources representing the metal/semiconductor contact (S_{IS}) and multiple interlayer resistances ($S_{I\mathrm{int}}$), along with the associated parallel resistances. To add such series sources, it is necessary to convert to Thévenin equivalent-resistance-noise sources, such as the one illustrated in Fig. 5(d). The overall noise-spectral-power density is $S_{R\mathrm{total}} = S_{R1} + S_{R\mathrm{ch}}$, where S_{R1} is expressed as $S_{R1} = S_{Rs} + n{\cdot}S_{R\mathrm{int}}$. The overall resistance can be obtained by adding the series-connected resistances. Because the contact resistance and interlayer-coupling resistance are not negligible, we model that both the contact and the interlayer resistances contribute to the measured noise.

In order to investigate the channel length dependence of the noise, we fabricate 8L $MoSe_2$ FETs with different channel lengths ($L_{\mathrm{ch}} = 0.5$, 1, and 2 μm) on the same flake. The dimensions and contact electrical parameters are presented in Table I. Figure 6 presents the measured noise amplitude vs ($V_{GS} - V_{\mathrm{th}}$) for the devices, along with the model (channel-noise term, contact-noise term, and total) corresponding to the 2-μm-channel length. The measured $(g_m/I_d)^2$ relationship is also shown for the 2-μm-channel length; as with the devices shown in Fig. 4, this relationship did not fit the experimental data as well as the model which considered the Hooge model and contact effects. Using comparable analysis to that described previously, values of S_{R1} and the Hooge parameter are extracted for the devices and presented in Table I. The observation of comparable Hooge parameters for devices with varying channel lengths is consistent with the behavior expected in a channel-dominated regime (as labeled in Fig. 6). Qualitatively similar results are also observed in 3L FETs with different channel lengths. (See Appendix E for more details). In order to allow direct comparison between devices with various channel lengths, the area scaling of noise in 3L and 8L FETs is presented in Appendix F. It is informative to compare the noise results in this study to both prior thickness-dependent mobility studies and noise studies. Prior studies have attributed the increasing mobility with increasing layer thickness to Thomas-Fermi screening, resulting in decreased scattering by interface states [26]. Since interface states are generally thought to be responsible for the noise, one would also expect a decreasing channel contribution to noise amplitude with increasing layer thickness. Noise amplitude can also be compared, e.g., to that of Paul et al. [43]. Although that study observed voltage-dependent noise that followed a carrier-density-fluctuation model, the noise amplitudes for few-layers devices for voltages just above the threshold (as defined in the current study) are comparable to those observed in the 3L and 5L devices at comparable overdrive

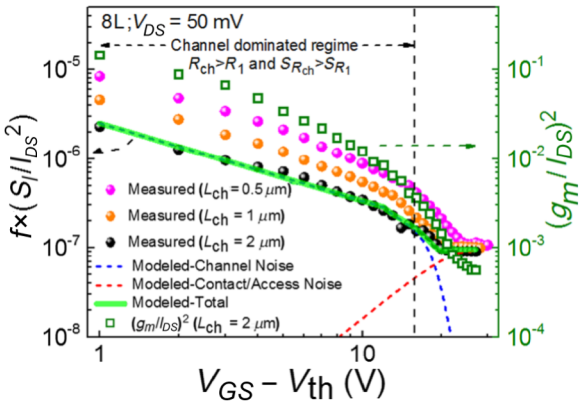

FIG. 6. The noise amplitudes $f \times S_I/I_{DS}^2$ and $(g_m/I_{DS})^2$ as a function of overdrive voltage in 8L $MoSe_2$ FETs. Pink, orange, and black circles represent the noise amplitude of $L_{\mathrm{ch}} = 0.5$, 1, and 2 μm, respectively. The blue (red) dashed line indicates the model fitting for the noise in the channel (contact) regime. Green opened square corresponds to $(g_m/I_{DS})^2$. Arrows indicate the appropriate axis.

voltages in the current study. The devices in the current study employ an approximately 3 times thinner SiO_2-gate dielectric, resulting in an approximately 3 times larger sheet-carrier density at a given overdrive voltage. Paul et al. inferred metallic-regime behavior for gate voltages corresponding to an overdrive voltage of approximately 3 V; for the devices in the current study, the sheet carrier density is at the corresponding level or higher for overdrive voltages above approximately 1 V.

Prior studies on FETs with TMDC channels have observed comparable behavior in the transition regions between channel-dominated and contact/access-dominated noise regimes [41,42]. In some cases, the transition has been interpreted as a change in the dominant-channel-noise mechanism from a mobility-fluctuation (Hooge) mechanism to a carrier-density fluctuation (McWhorter) mechanism, which would exhibit a V_{GS}^{-2} dependence [30,44]. However, the voltage dependence of the noise amplitude can be modeled using the channel and contact/access contributions discussed above, with a single physical model for the channel contribution. The voltage dependence in the transition region can be explained by the sequential transitions of resistance and noise from channel-dominated to contact-dominated regimes. Such a model is found to be valid across the full range of layer thicknesses considered in this study, with the same channel-noise mechanism in all devices.

IV. CONCLUSIONS

In conclusion, in the present work, we provide a comprehensive study of the correlation between the electrical transport and 1/f noise studies in $MoSe_2$ FETs with varying channel-layer thicknesses. The obtained

mobility vs layer thickness of $MoSe_2$ FETs can be understood in terms of an intrinsic component associated with the channel and a component attributed to contact/interlayer-coupling resistance, which both change with layer thickness. The gate-voltage dependence of the noise amplitude can be understood in terms of a voltage-dependent channel-dominated component and a voltage-independent contact/access-dominated regime. A quantitative model is developed which adequately describes the observed voltage dependence, and which allows extraction of channel vs contact/access parameters for each layer thickness. Although previous studies on multilayer TMDC FETs have attributed the voltage dependence of noise amplitude to a transition from Hooge noise mechanism to McWhorter behavior, a model considering both channel and contact/access-resistance contributions can fit the observed voltage dependence for devices across the full range of layer thicknesses using only one mechanism (Hooge's mobility fluctuation). The Hooge's constant (2.64×10^{-3}) extracted from the channel-dominated regime for the 15-layer device is comparable to values reported for reliable nanoscale FETs.

ACKNOWLEDGMENTS

J.K. and D.B.J. acknowledge funding support in part by National Science Foundation under Grant No. ECCS – 1408346. S.R.D. acknowledges start-up funding from the College of Engineering at Kansas State University.

APPENDIX A: DEVICE FABRICATION

Using a mechanical exfoliation technique, high-quality crystalline-$MoSe_2$ flakes (from 2D Semiconductor, Inc.) are transferred onto highly doped Si/SiO_2 wafers (SiO_2 thickness of 90 nm) with predefined alignment markers. $MoSe_2$ flakes are first identified using an optical microscope, and the thickness of each flake is determined using an AFM. FETs are fabricated using seven of the $MoSe_2$ flakes, with thicknesses listed in Table I, as the channel material. *SD* contact electrodes are defined by e-beam lithography (Raith e_LiNE) followed by 50-nm-nickel e-beam evaporation and liftoff.

A Keithley 4200 semiconductor parameter analyzer and probe station are used for the transport measurements and an Agilent Technologies 35670A dynamic signal analyzer, low-noise current preamplifier (Stanford Research SR570), and voltage source are used for the $1/f$ noise measurement. All the grounding terminals from the equipment are connected to an instrument-ground system.

APPENDIX B: EXTRACTION OF SERIES RESISTANCE FOR THE $MoSe_2$ FETS

The series resistance (R_1) is extracted from the measured device resistance vs gate voltage relationship by plotting the total resistance (R_{total}) vs $1/(V_{GS} - V_{th})$ and extrapolating the line to the y axis (Fig. 7). The extracted R_1 is employed for the analysis of mobility and noise parameters. For 15L and 40L, the series resistances are 21 and 187 kΩ, respectively.

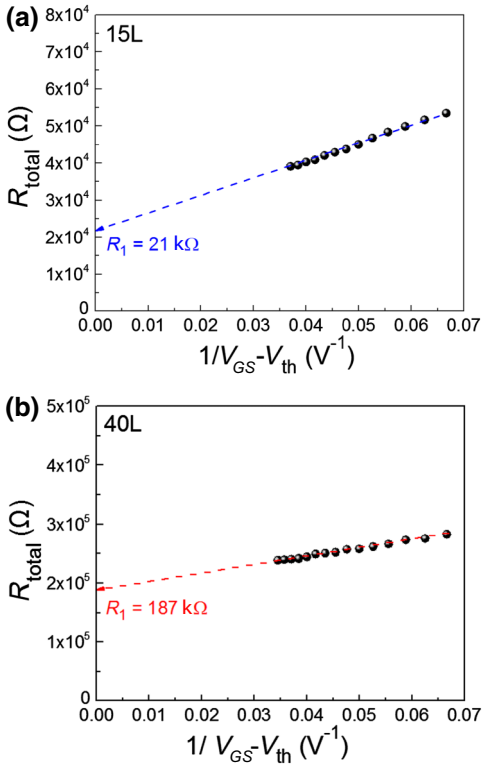

FIG. 7. Total resistance vs $1/(V_{GS} - V_{th})$ for the extraction of series resistance (a) 15L and (b) 40L.

APPENDIX C: EXTRACTION OF FIELD-EFFECT MOBILITY FOR $MoSe_2$ FETS

The transconductance is obtained by first-order differentiation of the transfer characteristic (Fig. 8). The

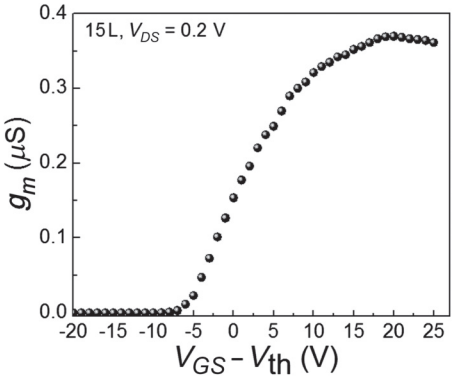

FIG. 8. Transconductance (g_m) as a function of the overdrive voltage ($V_{GS} - V_{th}$) at $V_{DS} = 0.2$ V for 15L $MoSe_2$ FET.

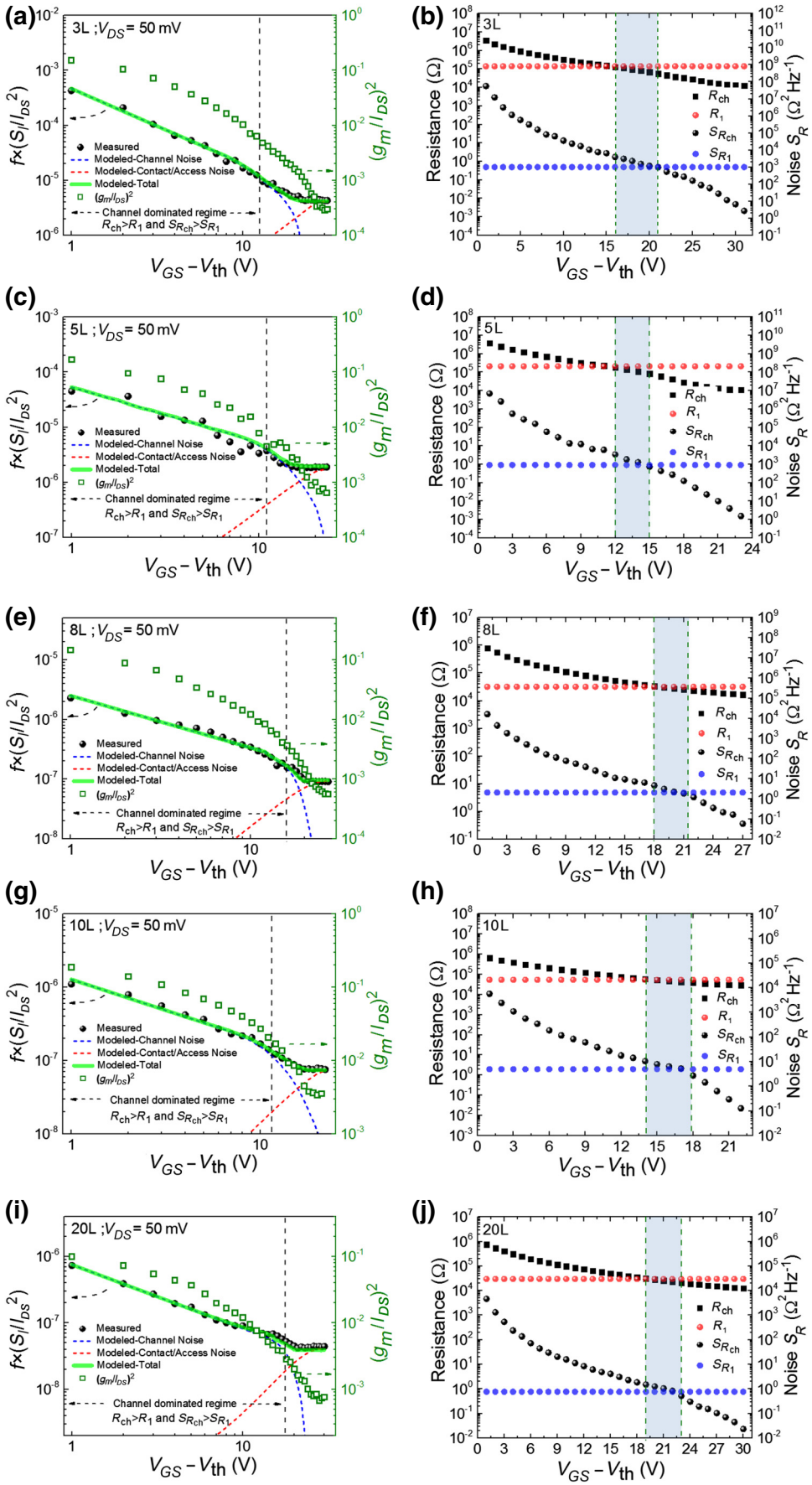

FIG. 9. (a), (c), (e), (g), and (i): Measured and modeled 1/f noise response of $MoSe_2$ FETs vs overdrive voltage. The round symbols represent the measured data points for the normalized noise-current-power-spectral density, $f \times S_I/I_{DS}^2$, as a function of the gate bias. The dashed lines represent the model fitting for the corresponding noise amplitude due to noise sources in the channel (blue) and the contact contribution (red). The green line shows the total modeled noise amplitude (sum of the two components). Green opened square corresponds to $(g_m/I_{DS})^2$ in the right-sided y axis. (b), (d), (f), (h), and (j): Contact and channel components of the resistance-noise-power density and resistance for $MoSe_2$ FET, obtained from measurements using procedure described in text. Blue area represents "transition regime" in which channel dominates noise, but contact/access regions dominate resistance. (a), (b) for 3L, (c), (d) for 5L, (e), (f) for 8L, (g), (h) for 10L, and (i), (j) for 20L.

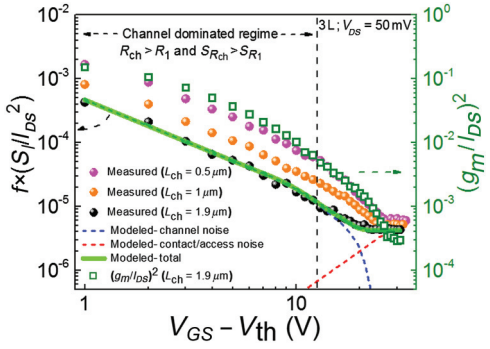

FIG. 10. The noise amplitudes $f \times S_I/I_{DS}^2$ and $(g_m/I_{DS})^2$ as a function of overdrive voltage in 3L $MoSe_2$ FETs. Pink, orange, and black circles represent the noise amplitude of $L_{ch.} = 0.5$, 1, and 1.9 μm, respectively. The blue (red) dashed line indicates the model fitting for the noise in the channel (contact) regime. Green opened square corresponds to $(g_m/I_{DS})^2$. Arrows indicate the appropriate axis.

peak g_m is then used to calculate the extrinsic field-effect mobility, which is obtained by using the equation $\mu_{ext} = (dI_{DS}/dV_{GS}) \times (L/W) \times (1/C_{ox}) \times (1/V_{DS})$.

APPENDIX D: NOISE AMPLITUDE AND NOISE/RESISTANCE COMPONENTS IN $MoSe_2$ FETS WITH VARIOUS NUMBERS OF LAYERS

The measured and modeled noise amplitudes are presented in Fig. 9 for FETs with various layer thicknesses (15L and 40L results presented in main article). For each device, the $f \times S_I/I_{DS}^2$ is shown vs $(V_{GS} - V_{th})$ and the resistances and noise-resistance-spectral-power densities associated with channel and contact/access regions are presented.

APPENDIX E: NOISE AMPLITUDE AND $(g_m/I_{ds})^2$ IN 3L $MoSe_2$ FETS WITH VARIOUS CHANNEL LENGTHS

Figure 10 shows the channel length variation of measured, modeled, and total noise of $MoSe_2$ FETs with 3-atomic layer channel thicknesses. The channel lengths and widths are kept similar to the ones showed in case of 8-layer FETs (Fig. 6). Same drain bias of 50 mV is applied to these devices.

APPENDIX F: THE AREA DEPENDENCE OF NOISE IN 3L AND 8L $MoSe_2$ FETS

In order to verify that the noise amplitude scales as expected with area in the channel-dominated regime, the area dependence of noise for 3L and 8L FETs is presented in this section. Figure 11 shows the noise parameter multiplied by area (Area $\times S_I/I_{DS}^2$) vs the overdrive voltage $(V_{GS} - V_{th})$ in 3L and 8L FETs. For each set of devices, the curves for various channel lengths are comparable in the channel-dominated regime (at the low overdrive voltages), but reach different limiting values in the contact-dominated regime (at high overdrive voltages).

TABLE II. The parameters showing electrical properties and noise phenomenon in 3L $MoSe_2$ FETs with different channel lengths.

No. of layers	$L_{ch} \times W_{ch}$ (μm^2)	R_1 (kΩ)	$R_1 \times W_{ch}$ (kΩ μm)	V_{th} (V)	S_{R1} (Ω^2/Hz)	α_H
3L	0.5×4	43	172	7	197.5	8.41×10^{-1}
3L	1×4	65	260	8	422	8.17×10^{-1}
3L	1.9×3	141	423	9	1014	7.08×10^{-1}

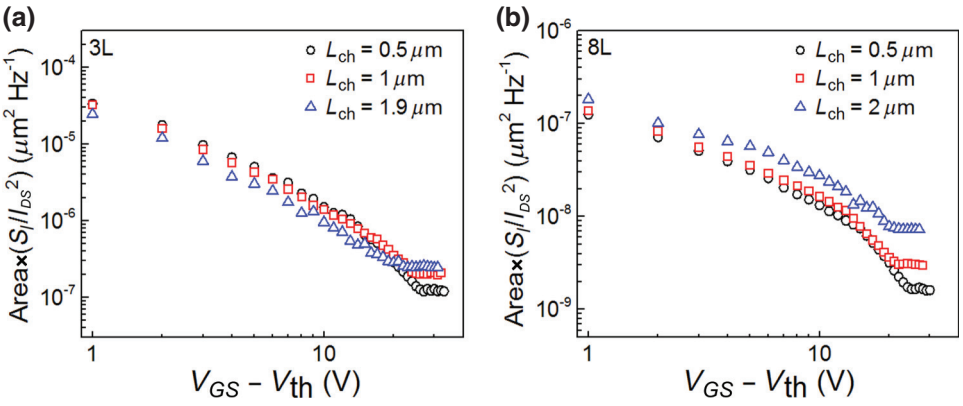

FIG. 11. The noise parameter (Area $\times S_I/I_{DS}^2$) as a function of overdrive voltage in (a) 3L and (b) 8L $MoSe_2$ FETs. Black circle, red square, and blue triangle represent the noise parameters of $L_{ch} = 0.5$ μm (0.5 μm), 1 μm (1 μm), and 1.9 μm (2 μm) in 3L (8L) $MoSe_2$ FETs, respectively.

[1] K. S. Novoselov, F. S. D. Jiang, T. J. Booth, V. V. Khotkevich, S. V. Morozov, and A. K. Geim, Two-dimensional atomic crystals, PNAS **102**, 10451 (2005).

[2] B. Radisavljevic, J. B. A. Radenovic, V. Giacometti, and A. Kis, Single-layer MoS_2 transistors, Nat. Nanotechnol. **6**, 147 (2011).

[3] O. Lopez-Sanchez, D. Lembke, M. Kayci, A. Radenovic, and A. Kis, Ultrasensitive photodetectors based on monolayer MoS_2, Nat. Nanotechnol. **8**, 497 (2013).

[4] F. Xia, H. Wang, D. Xiao, M. Dubey, and A. Ramasubramaniam, Two-dimensional material nanophotonics, Nat. Photonics **8**, 899 (2014).

[5] K. F. Mak, C. Lee, J. Hone, J. Shan, and T. F. Heinz, Atomically Thin MoS_2 A New Direct-Gap Semiconductor, Phys. Rev. Lett. **105**, 136805 (2010).

[6] A. Splendiani, L. Sun, Y. Zhang, T. Li, J. Kim, C. Y. Chim, G. Galli, and F. Wang, Emerging photoluminescence in monolayer MoS_2, Nano Lett. **10**, 1271 (2010).

[7] A. Anedda and E. Fortin, Exciton spectra in $MoSe_2$, J. Phys. Chem. Solids **41**, 865 (1980).

[8] D. Y. Qiu, F. H. Da Jornada, and S. G. Louie, Optical Spectrum of MoS_2: Many-Body Effects and Diversity of Exciton States, Phys. Rev. Lett. **111**, 1 (2013).

[9] K. F. Mak, K. He, C. Lee, G. H. Lee, J. Hone, T. F. Heinz, and J. Shan, Tightly bound trions in monolayer MoS_2, Nat. Mater. **12**, 207 (2012).

[10] A. Prakash, H. Ilatikhameneh, P. Wu, and J. Appenzeller, Understanding contact gating in Schottky barrier transistors from 2D channels, Sci. Rep. **7**, 1 (2017).

[11] W. Zhao, R. M. Ribeiro, M. Toh, A. Carvalho, C. Kloc, A. H. Castro Neto, and G. Eda, Origin of indirect optical transitions in few-layer MoS_2, Nano Lett. **13**, 5627 (2013).

[12] I. G. Lezama, A. Arora, A. Ubaldini, C. Barreteau, E. Giannini, M. Potemski, and A. F. Morpurgo, Indirect-to-direct band gap crossover in few-layer $MoTe_2$, Nano Lett. **15**, 2336 (2015).

[13] A. Kumara and P. K. Ahluwalia, Electronic structure of transition metal dichalcogenides monolayers 1H-MX_2 (M = Mo, W; X = S, Se, Te) from ab-initio theory: New direct band gap semiconductors, Eur. Phys. J. B **85**, 186 (2012).

[14] J. Kang, L. Zhang, and S. H. Wei, A unified understanding of the thickness-dependent bandgap transition in hexagonal two-dimensional semiconductors, J. Phys. Chem. Lett. **7**, 597 (2016).

[15] Q. H. Wang, K. Kalantar-Zadeh, A. Kis, J. N. Coleman, and M. S. Strano, Electronics and optoelectronics of two-dimensional transition metal dichalcogenides, Nat. Nanotechnol. **7**, 699 (2012).

[16] W. Wu, D. De, S. C. Chang, Y. Wang, H. Peng, J. Bao, and S. S. Pei, High mobility and high on/off ratio field-effect transistors based on chemical vapor deposited single-crystal MoS_2 grains, Appl. Phys. Lett. **102**, 142106 (2013).

[17] S. Das, H.-Y. Chen, A. V. Penumatcha, and J. Appenzeller, High performance multilayer MoS_2 transistors with scandium contacts, Nano Lett. **13**, 100 (2013).

[18] Y. Yoon, K. Ganapathi, and S. Salahuddin, How good can monolayer MoS_2 transistors be?, Nano Lett. **11**, 3768 (2011).

[19] S. Larentis, B. Fallahazad, and E. Tutuc, Field-effect transistors and intrinsic mobility in ultra-thin $MoSe_2$ layers, Appl. Phys. Lett. **101**, 223104 (2012).

[20] H. Wang, L. Yu, Y.-H. Lee, Y. Shi, A. Hsu, M. L. Chin, L.-J. Li, M. Dubey, J. Kong, and T. Palacios, Integrated circuits based on bilayer MoS_2 transistors, Nano Lett. **12**, 4674 (2012).

[21] B. Radisavljevic, M. B. Whitwick, and A. Kis, Integrated circuits and logic operations based on single-layer MoS_2, ACS Nano **5**, 9934 (2011).

[22] H. Wang, L. Yu, Y.-H. Lee, W. Fang, A. Hsu, P. Herring, M. Chin, M. Dubey, L.-J. Li, J. Kong, and T. Palacios, Large-scale 2D electronics based on single-layer MoS_2 grown by chemical vapor deposition, Int. Electron Devices Meet. **6**, 4.6.1 (2012).

[23] A. Sanne, R. Ghosh, A. Rai, M. N. Yogeesh, S. H. Shin, A. Sharma, K. Jarvis, L. Mathew, R. Rao, D. Akinwande, and S. Banerjee, Radio frequency transistors and circuits based on CVD MoS_2, Nano Lett. **15**, 5039 (2015).

[24] G. Fiori, F. Bonaccorso, G. Iannaccone, T. Palacios, D. Neumaier, A. Seabaugh, S. K. Banerjee, and L. Colombo, Electronics based on two-dimensional materials, Nat. Nanotechnol. **9**, 768 (2014).

[25] N. R. Pradhan, D. Rhodes, Y. Xin, S. Memaran, L. Bhaskaran, M. Siddiq, S. Hill, P. M. Ajayan, and L. Balicas, Ambipolar molybdenum diselenide field-effect transistors: Field-effect and hall mobilities, ACS Nano **8**, 7923 (2014).

[26] S. Das and J. Appenzeller, Screening and interlayer coupling in multilayer MoS_2, Rapis Res. Lett. **7**, 268 (2013).

[27] S. Xu, Z. Wu, H. Lu, Y. Han, G. Long, X. Chen, T. Han, W. Ye, Y. Wu, J. Lin, J. Shen, Y. Cai, Y. He, F. Zhang, R. Lortz, C. Cheng, and N. Wang, Universal low-temperature Ohmic contacts for quantum transport in transition metal dichalcogenides, 2D Mater. **3**, 021007 (2016).

[28] F. Giannazzo, G. Fisichella, A. Piazza, S. Di Franco, G. Greco, S. Agnello, and F. Roccaforte, Impact of contact resistance on the electrical properties of MoS_2 transistors at practical operating temperatures, Beilstein J. Nanotechnol. **8**, 254 (2017).

[29] F. N. N. Hooge, 1 / F Noise Sources, IEEE Trans. Electron Devices **41**, 1926 (1994).

[30] L. K. J. Vandamme and F. N. Hooge, On the additivity of generation-recombination spectra Part 3: The McWhorter model for 1/f noise in MOSFETs, Phys. B Condens. Matter. **357**, 507 (2005).

[31] L. K. J. Vandamme, X. Li, and D. Rigaud, 1/f noise in MOS devices, mobility or number fluctuationsâĂŕ?, IEEE Trans. Electron Devices **41**, 1936 (1994).

[32] C. J. Delker, Y. Zi, C. Yang, and D. B. Janes, Low-frequency noise contributions from channel and contacts in InAs nanowire transistors, IEEE Trans. Electron Devices **60**, 2900 (2013).

[33] S. Kim, P. D. Carpenter, R. K. Jean, H. Chen, C. Zhou, S. Ju, and D. B. Janes, Role of self-assembled monolayer passivation in electrical transport properties and flicker noise of nanowire transistors, ACS Nano **6**, 7352 (2012).

[34] N. Clément, K. Nishiguchi, A. Fujiwara, and D. Vuillaume, One-by-one trap activation in silicon nanowire transistors, Nat. Commun. **1**, 92 (2010).

[35] F. Liu, K. L. Wang, D. Zhang, and C. Zhou, Noise in carbon nanotube field effect transistor, Appl. Phys. Lett. **89**, 12 (2006).

[36] A. A. Balandin, Low-frequency 1/f noise in graphene devices, Nat. Nanotechnol. **8**, 549 (2013).

[37] V. K. Sangwan, H. N. Arnold, D. Jariwala, T. J. Marks, L. J. Lauhon, and M. C. Hersam, Low-frequency electronic noise in single-layer MoS_2 transistors, Nano Lett. **13**, 4351 (2013).

[38] X. Xie, D. Sarkar, W. Liu, J. Kang, O. Marinov, M. Jamal Deen, and K. Banerjee, Low-frequency noise in bilayer MoS_2 transistor, ACS Nano **8**, 5633 (2014).

[39] Y. M. Lin and P. Avouris, Strong suppression of electrical noise in bilayer graphene nanodevices, Nano Lett. **8**, 2119 (2008).

[40] K. Hsieh, V. Kochat, X. Zhang, Y. Gong, C. S. Tiwary, P. M. Ajayan, and A. Ghosh, Effect of carrier localization on electrical transport and noise at individual grain boundaries in monolayer MoS_2, Nano Lett. **17**, 5452 (2017).

[41] J. Na, M.-K. Joo, M. Shin, J. Huh, J.-S. Kim, M. Piao, J.-E. Jin, H.-K. Jang, H. J. Choi, J. H. Shim, and G.-T. Kim, Low-frequency noise in multilayer MoS_2 field-effect transistors: the effect of high-k passivation, Nanoscale **6**, 433 (2014).

[42] D. Sharma, A. Motayed, P. B. Shah, M. Amani, M. Georgieva, A. Glen Birdwell, M. Dubey, Q. Li, and A. V. Davydov, Transfer characteristics and low-frequency noise in single- and multi-layer MoS_2 field-effect transistors, Appl. Phys. Lett. **107**, 1 (2015).

[43] T. Paul, S. Ghatak, and A. Ghosh, Percolative switching in transition metal dichalcogenide field-effect transistors at room temperature, Nanotechnology **27**, 125706 (2016).

[44] J. Renteria, R. Samnakay, S. L. Rumyantsev, C. Jiang, P. Goli, M. S. Shur, and A. A. Balandin, Low-frequency 1/f noise in MoS_2 transistors: Relative contributions of the channel and contacts, Appl. Phys. Lett. **104**, 1 (2014).

[45] X. Li, L. Yang, M. Si, S. Li, M. Huang, P. Ye, and Y. Wu, Performance potential and limit of MoS_2 transistors, Adv. Mater. **27**, 1547 (2015).

[46] D. Sharma, M. Amani, A. Motayed, P. B. Shah, A. G. Birdwell, S. Najmaei, P. M. Ajayan, J. Lou, M. Dubey, Q. Li, and A. V. Davydov, Electrical transport and low-frequency noise in chemical vapor deposited single-layer MoS_2 devices, Nanotechnology **25**, 155702 (2014).

[47] H. J. Kwon, H. Kang, J. Jang, S. Kim, and C. P. Grigoropoulos, Analysis of flicker noise in two-dimensional multilayer MoS_2 transistors, Appl. Phys. Lett. **104**, 8 (2014).

[48] I. Martinez, M. Ribeiro, P. Andres, L. E. Hueso, F. Casanova, and F. G. Aliev, Photodoping-Driven Crossover in the Low-Frequency Noise of MoS_2 Transistors, Phys. Rev. Appl. **7**, 034034 (2017).

[49] S. R. Das, J. Kwon, A. Prakash, C. J. Delker, S. Das, and D. B. Janes, Low-frequency noise in $MoSe_2$ field effect transistors, Appl. Phys. Lett. **106**, 083507 (2015).

[50] F. K. Perkins, A. L. Friedman, E. Cobas, P. M. Campbell, G. G. Jernigan, and B. T. Jonker, Chemical vapor sensing with monolayer MoS_2, Nano Lett. **13**, 668 (2013).

[51] S. Lee and Z. Zhong, Nanoelectronic circuits based on two-dimensional atomic layer crystals, Nanoscale **6**, 13283 (2014).

[52] Branimir Radisavljevic, M. B. Whitwick, and Andras Kisa, Small-signal amplifier based on single-layer MoS_2, Appl. Phys. Lett. **101**, 043103 (2012).

[53] J. O. Island, A. Kuc, E. H. Diependaal, R. Bratschitsch, H. S. J. van der Zant, T. Heine, and A. Castellanos-Gomez, Precise and reversible band gap tuning in single-layer $MoSe_2$ by uniaxial strain, Nanoscale **8**, 2589 (2016).

[54] Y. Zhang, T.-R. Chang, B. Zhou, Y.-T. Cui, H. Yan, Z. Liu, F. Schmitt, J. Lee, R. Moore, Y. Chen, H. Lin, H.-T. Jeng, S.-K. Mo, Z. Hussain, A. Bansil, and Z.-X. Shen, Direct observation of the transition from indirect to direct bandgap in atomically thin epitaxial $MoSe_2$, Nat. Nanotechnol. **9**, 111 (2014).

[55] S. Tongay, J. Zhou, C. Ataca, K. Lo, T. S. Matthews, J. Li, J. C. Grossman, and J. Wu, Thermally driven crossover from indirect toward direct bandgap in 2D semiconductors: $MoSe_2$ versus MoS_2, Nano Lett. **12**, 5576 (2012).

[56] S. K. Mahatha, K. D. Patel, and K. S. R. Menon, Electronic structure investigation of MoS_2 and $MoSe_2$ using angle-resolved photoemission spectroscopy and ab initio band structure studies, J. Phys. Condens. Matter **24**, 475504 (2012).

[57] Y. H. Chang, W. Zhang, Y. Zhu, Y. Han, J. Pu, J. K. Chang, W. T. Hsu, J. K. Huang, C. L. Hsu, M. H. Chiu, T. Takenobu, H. Li, C. I. Wu, W. H. Chang, A. T. S. Wee, and L. J. Li, Monolayer $MoSe_2$ grown by chemical vapor deposition for fast photodetection, ACS Nano **8**, 8582 (2014).

[58] Y. Guo, D. Liu, and J. Robertson, Chalcogen vacancies in monolayer transition metal dichalcogenides and Fermi level pinning at contacts, Appl. Phys. Lett. **106**, 173106 (2015).

[59] W. Liao, W. Wei, Y. Tong, W. K. Chim, and C. Zhu, Electrical performance and low frequency noise in hexagonal boron nitride encapsulated $MoSe_2$ dual-gated field effect transistors, Appl. Phys. Lett. **111**, 082105 (2017).

[60] J. S. Ross, S. Wu, H. Yu, N. J. Ghimire, A. M. Jones, G. Aivazian, J. Yan, D. G. Mandrus, D. Xiao, W. Yao *et al.*, Electrical control of neutral and charged excitons in a monolayer semiconductor, Nat. Commun. **4**, 1474 (2013).

[61] J. Rhayem, M. Valenza, D. Rigaud, N. Szydlo, and H. Lebrun, 1/F noise investigations in small channel length amorphous silicon thin film transistors, J. Appl. Phys. **83**, 3660 (1998).

[62] S. Ghatak, A. N. Pal, and A. Ghosh, Nature of electronic states in atomically thin MoS_2 field-effect transistors, ACS Nano **5**, 7707 (2011).

[63] S. Das and J. Appenzeller, Where does the current flow in two- dimensional layered systems?, Nano Lett. **13**, 3396 (2013).

[64] C. J. Delker, S. Kim, M. Borg, L. E. Wernersson, and D. B. Janes, 1/F noise sources in dual-gated indium arsenide nanowire transistors, IEEE Trans. Electron Devices **59**, 1980 (2012).

[65] G. Liu, S. Rumyantsev, M. S. Shur, and A. A. Balandin, Origin of 1/f noise in graphene multilayers: Surface vs. volume, Appl. Phys. Lett. **102**, 093111 (2013).